

1 INTRODUCTION

2 Above Earth's atmosphere are the a pair of Van Allen radiation belts, a complex
3 and dynamic plasma environment that affects our technology-driven society. These
4 effects include: a higher radiation dose for astronauts and cosmonauts, higher chance
5 of spacecraft failure due to single event upsets that can lead to catastrophic latchups,
6 degradation of silicon (changing the silicon doping) from an extended radiation dose
7 that can degrade a transistor to the point where it no longer function as a switch,
8 and the degradation of the ozone layer due to the chemical production of NO_X and
9 HO_X molecules. With these effects in mind, it is no surprise that the radiation belts
10 have been extensively studied since their discovery in the 1960s.

11 One natural phenomenon in the radiation belts that has been a topic of interest
12 in the space physics community is wave-particle interactions that, as we will explore
13 throughout this dissertation, can accelerate particles to very high energies (e.g. \approx
14 MeV for electrons) and scatter them into the atmosphere.

15 The goal of this dissertation is to study the wave-particle scattering mechanism
16 that scatters electron microbursts. Electron microbursts, henceforth referred to
17 as microbursts, are typically observed by low Earth orbiting spacecraft, sounding
18 rockets, and high altitude balloons as a sub-second impulse of electrons. Some of
19 the most intense microbursts are observed as a 10 to 100 fold increase of electrons
20 (for example see Fig. 7 in Blake et al. (1996)). Since they were first reported by
21 Anderson and Milton (1964), the short microburst duration and their impulsive nature
22 have compelled countless researchers to understand their properties and the physical
23 mechanism(s) that create microbursts. Microbursts are widely believed to be created
24 by wave-particle scattering between a plasma wave called whistler mode chorus
25 and outer radiation belt electrons, although many details regarding the scattering

²⁶ mechanism are unconstrained or unknown.

²⁷ This chapter serves as an introduction to the physics of charged particles, plasma
²⁸ waves, and the wave-particle interactions in Earth's magnetosphere. We will first
²⁹ derive the motion of individual charged particles in Earth's electric and magnetic
³⁰ fields. Then we will cover how various groups of charged particles coalesce to form
³¹ the major particle populations in the magnetosphere. Then, we will cover the various
³² mechanisms that accelerate particles in the magnetosphere. Lastly, we will review
³³ the basics of microbursts as a jumping-off point for the rest of the dissertation.

³⁴ Charged Particle Motion in Electric and Magnetic Fields

A charged particle trapped in the magnetosphere will experience three types of periodic motion in Earth's nearly dipolar magnetic field. The three motions are ultimately due to the Lorentz force that a particle of momentum \vec{p} , charge q , and velocity \vec{v} experiences in an electric field \vec{E} and magnetic field \vec{B} and is given by

$$\frac{d\vec{p}}{dt} = q(\vec{E} + \vec{v} \times \vec{B}). \quad (1.1)$$

³⁵ In the magnetosphere, the three periodic motions, in decreasing frequency, are
³⁶ gyration, bounce, and drift and are schematically shown in Fig. 1.1. Each of periodic
³⁷ these motions have a corresponding conserved quantity i.e. an adiabatic invariant.

The highest frequency periodic motion is gyration about a magnetic field of magnitude B . This motion is circular with a Larmor radius of

$$r = \frac{mv_{\perp}}{|q|B} \quad (1.2)$$

where m is the mass and v_{\perp} the particle's velocity perpendicular to \vec{B} . This motion

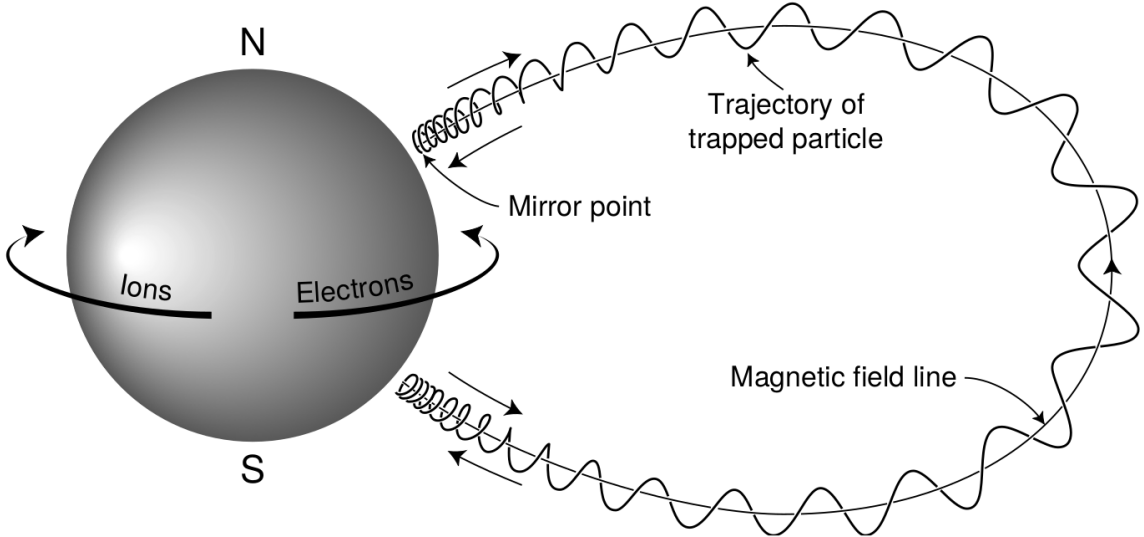


Figure 1.1: The three periodic motions of charged particles in Earth's dipole magnetic field. These motions are: gyration about the magnetic field line, bounce motion between the magnetic poles, and azimuthal drift around the Earth. Figure from (Baumjohann and Treumann, 1997).

has a corresponding gyrofrequency

$$\Omega = \frac{|q|B}{m} \quad (1.3)$$

in units of radians/second. Inside the radiation belts the electron gyrofrequency, Ω_e is on the order of a kHz. The corresponding adiabatic invariant is found by integrating the particle's canonical momentum around the particle's path of gyration

$$J_i = \oint (\vec{p} + q\vec{A}) \cdot d\vec{l} \quad (1.4)$$

³⁸ where J_i is the i^{th} adiabatic invariant and \vec{A} is the magnetic vector potential. This
³⁹ integral is carried out by integrating the first term over the circumference of the gyro
⁴⁰ orbit and integrating the second term using Stokes theorem to calculate the magnetic
⁴¹ flux enclosed by the gyro orbit. The gyration invariant is then $J_1 \sim v_{\perp}^2/B$, which is

⁴² conserved when the frequency, ω of a force acting on the gyrating electron satisfies
⁴³ $\omega \ll \Omega_e$.

⁴⁴ The second highest frequency periodic motion is bouncing due to a parallel
⁴⁵ gradient in \vec{B} . This periodic motion naturally arises in the magnetosphere because
⁴⁶ Earth's magnetic field is stronger near the poles, and artificially in the laboratory
⁴⁷ in magnetic bottle machines. To understand this motion we first we need to define
⁴⁸ the concept of pitch angle α as the angle between \vec{B} and \vec{v} which is schematically
⁴⁹ shown in Fig. 1.2a. The pitch angle relates v with v_{\perp} , and v_{\parallel} (the component of the
⁵⁰ particles velocity parallel to \vec{B}). As shown in 1.2b and c, a smaller (larger) α will
⁵¹ increase (decrease) the distance that the charged particle travels parallel to \vec{B} , during
⁵² one gyration.

Assuming the particle's kinetic energy is conserved, the conservation of J_1 implies that given a particle's $v_{\perp}(0)$ and $B(0)$ at the magnetic equator (where Earth's magnetic field is usually at a minimum), we can calculate its $v_{\perp}(s)$ along the particle's path s by calculating $B(s)$ from magnetic field models. The particle's perpendicular velocity is then related via

$$\frac{v_{\perp}^2(0)}{B(0)} = \frac{v_{\perp}^2(s)}{B(s)} \quad (1.5)$$

⁵³ which can be rewritten as

$$\frac{v^2 \sin^2 \alpha(0)}{B(0)} = \frac{v^2 - v_{\parallel}^2(s)}{B(s)} \quad (1.6)$$

⁵⁴ and re-arranged to solve for $v_{\parallel}(s)$

$$v_{\parallel}(s) = v \sqrt{1 - \frac{B(s)}{B(0)} \sin^2 \alpha(0)} \quad (1.7)$$

⁵⁵ which will tend towards 0 when the second term in the radical approaches 1.

56 The location where $v_{||}(s) = 0$ is called the mirror point and is where a particle
 57 reverses direction. Since Earth's magnetic field is stronger towards the poles, the
 58 mirroring particle will execute periodic bounce motion between its two mirror points
 59 in the northern and southern hemispheres. The corresponding adiabatic invariant, J_2
 60 is

$$J_2 = \oint p_{||} ds \quad (1.8)$$

where ds describes the particle path between the mirror points in the northern and southern hemispheres (see Fig. 1.1). J_2 is found by substituting Eq. 1.7 into Eq. 1.8 and defining the magnetic field strength at the mirror points as B_m where $\alpha(m) = 90^\circ$.

The J_2 integral can be written as

$$J_2 = 2p \int_{m_n}^{m_s} \sqrt{1 - \frac{B(s)}{B(m)}} ds \quad (1.9)$$

61 where m_n and m_s are the northern and southern mirror points, respectively. The
 62 bounce period can be estimated (e.g. Baumjohann and Treumann, 1997) to be

$$t_b \approx \frac{LR_e}{\sqrt{W/m}} (3.7 - 1.6 \sin \alpha(0)) \quad (1.10)$$

63 where L is the L -shell which describes the distance from the Earth's center to the
 64 location where a particular magnetic field line crosses the magnetic equator, in units
 65 of Earth radii, R_e . W is the particle's kinetic energy. As with gyration, the particle
 66 will bounce between the mirror points as long as $\omega \ll \Omega_b$, where Ω_b is the bounce
 67 frequency.

68 At this stage it is instructional to introduce the notion of the loss cone pitch
 69 angle, α_L . A particle with $\alpha \leq \alpha_L$ will mirror at or below ≈ 100 km altitude in

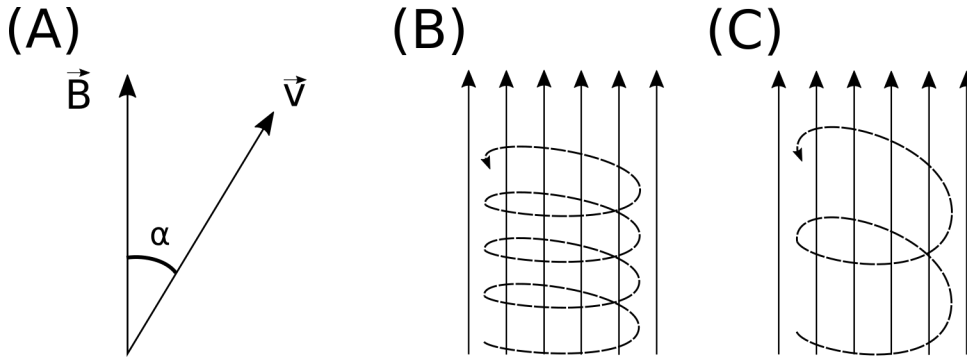


Figure 1.2: Charged particle motion in a uniform magnetic field \vec{B} . Panel (A) shows the geometry defining the pitch angle, α . Panel (B) and (C) show two helical electron trajectories with dashed lines assuming a large and small α (corresponding to a small and large parallel velocity $v_{||}$), respectively.

70 the atmosphere. A charged particle gyrating at those altitudes will encounter and
71 Coulomb scatter with the dense atmosphere and be lost from the magnetosphere.

72 The slowest periodic motion experienced by charged particles in Earth's mag-
73 netic field is azimuthal drift around the Earth. This drift results from a combination of
74 a radial gradient in \vec{B} and the curvature of the magnetic field. The radial gradient drift
75 arises because Earth's magnetic field is stronger near the Earth where the particle's
76 gyroradius radius of curvature is smaller as it gyrates towards stronger magnetic field,
77 and larger when it gyrates outward. The overall effect is the particle gyro orbit does
78 not close on itself and negatively charged particles drift east and positively charged
79 particles drift west. The radial gradient drift is enhanced by the centrifugal force that
80 a particle experiences as it bounces along the curved field lines. The drift adiabatic
81 invariant, J_3 is found by integrating Eq. 1.4 over the complete particle orbit around
82 the Earth. The shape of this drift orbit is otherwise known as a drift shell. For J_3 ,
83 the first term is negligible and the second term is the magnetic flux enclosed by the
84 drift shell, Φ_m i.e. $J_3 \sim \Phi_m$.

85 Figure 1.3 from Schulz and Lanzerotti (1974) shows contours of the gyration,

⁸⁶ bounce, and drift frequencies for electrons and protons in Earth's dipole magnetic
⁸⁷ field.

Up until now we have considered the three periodic motions due Earth's magnetic field and the absence of electric fields. If \vec{E} is present, a particle's center of gyration i.e., averaged position of the particle over a gyration, will drift with a velocity perpendicular to both \vec{E} and \vec{B} . The drift velocity can be solved directly from Eq. 1.1 and is

$$\vec{v}_E = \frac{\vec{E} \times \vec{B}}{B^2}. \quad (1.11)$$

⁸⁸ Lastly, for more detailed derivations of these motions, see the following texts:
⁸⁹ Baumjohann and Treumann (1997); Schulz and Lanzerotti (1974); Tsurutani and
⁹⁰ Lakhina (1997).

⁹¹ Particle Populations and Their Interractions in the Magnetosphere

⁹² Now that we have looked at the dynamics of single-particle motion in electric
⁹³ and magnetic fields, we will briefly tour the various macroscopic populations in the
⁹⁴ magnetosphere that are illustrated in Fig. 1.4.

⁹⁵ The sun and its solar wind are ultimately the source of energy input into the
⁹⁶ magnetosphere. The solar wind at Earth's orbit is a plasma traveling at supersonic
⁹⁷ speeds with an embedded interplanetary magnetic field (IMF). When the solar wind
⁹⁸ encounters Earth's magnetic field, the plasma can not easily penetrate into the
⁹⁹ magnetosphere because the plasma is frozen-in on magnetic field lines. Thus the
¹⁰⁰ plasma and its magnetic field drapes around the magnetosphere forming a cavity in
¹⁰¹ the solar wind that is roughly shaped as shown in Fig. 1.4. Because the solar wind
¹⁰² is supersonic at 1 AU, a bow shock exists upstream of the magnetosphere. The solar
¹⁰³ wind plasma, after it is shocked by the bow shock, flows around the magnetosphere

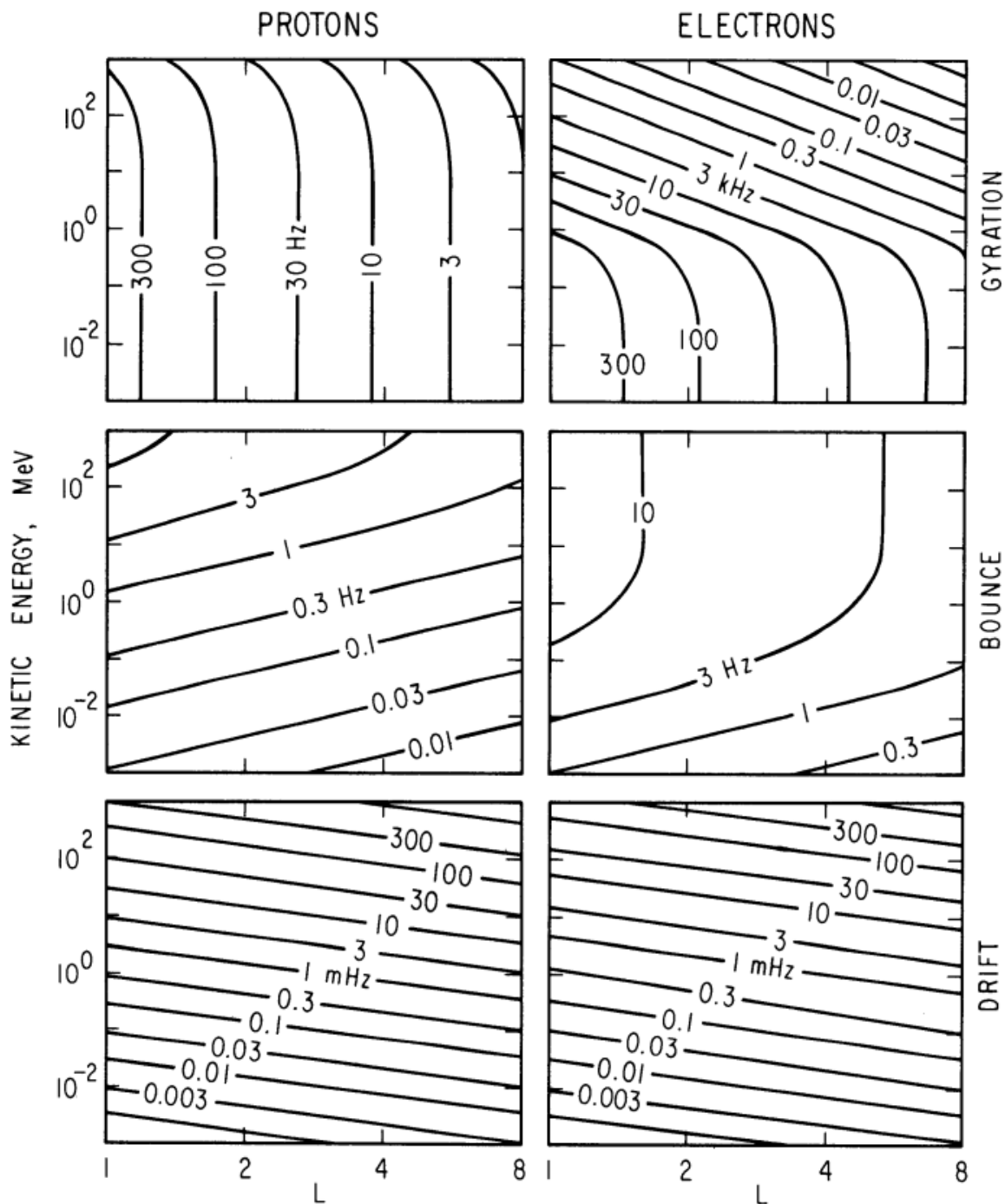


Figure 1.3: Contours of constant gyration, bounce, and drift frequencies for electrons and protons in a dipole field. Figure from Schulz and Lanzerotti (1974).

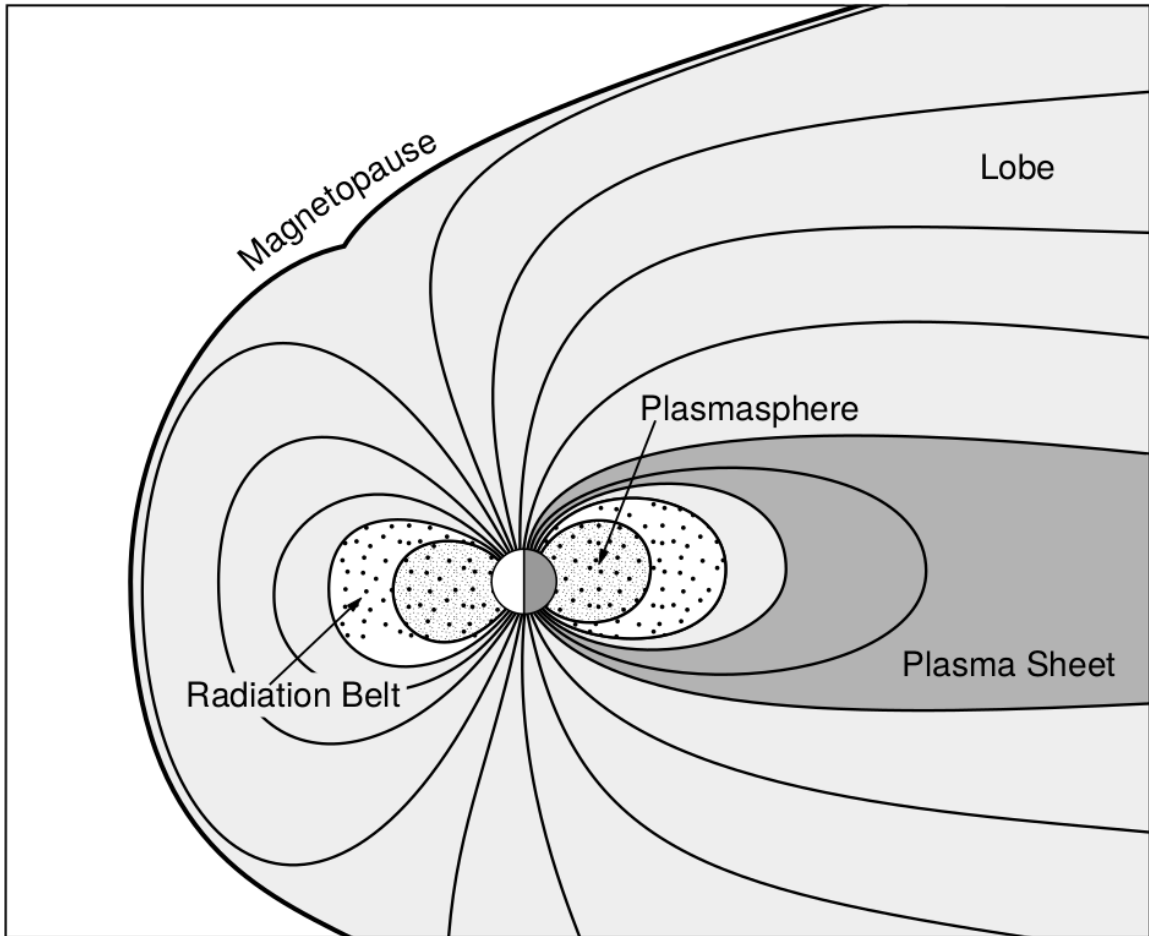


Figure 1.4: Macroscopic structures in the inner magnetosphere most relevant to this dissertation. The plasmasphere, and the radiation belts are shown and ring current is co-located there as well. Figure from Baumjohann and Treumann (1997).

104 inside the magnetosheath. The surface where the solar wind ram pressure and Earth's
 105 magnetic pressure balance is termed the magnetopause, which can be thought of as
 106 a boundary between the solar wind's and Earth's plasma environments. This is
 107 a slightly naive description of the magnetopause, but is nonetheless an instructive
 108 conceptual picture. The shocked plasma then flows past the Earth where it shapes
 109 the magnetotail. In the magnetotail the solar wind magnetic pressure balances Earth's
 110 magnetic field pressure in the lobes. The magnetotail extends on the order of 100
 111 R_E downstream of Earth, and the tailward stretching of magnetic field lines creates
 112 the plasma sheet which exists in the region of low magnetic field strength near the
 113 magnetic equator (e.g. Eastwood et al., 2015).

114 Populations in the Inner Magnetosphere

115 Closer to Earth, where the magnetic field is largely dipolar, are three plasma
 116 populations that comprise the inner magnetosphere: the plasmasphere, the ring
 117 current, and the radiation belts. Before we describe these three particle populations
 118 in detail, we will first introduce the coordinate system that most naturally describes
 119 the inner magnetosphere environment, and the electric fields that affect mostly low
 120 energy particles.

121 In this coordinate system the “radial” coordinate was defined in section 1 and
 122 is the L shell. The azimuthal coordinate is the magnetic local time (MLT). For an
 123 observer above Earth's north pole looking down, MLT is defined to be 0 (midnight)
 124 in the anti-sunward direction, and increases in the counter-clockwise direction with 6
 125 at dawn, 12 at noon (sunward direction), and 18 in dusk. The final coordinate is the
 126 magnetic latitude, λ which is analogous to the latitude coordinate in the spherical
 127 coordinate system, and is defined to be 0 at the magnetic equator. This coordinate
 128 system naturally describes the following inner magnetosphere populations.

129 The low energy particle dynamics in the inner magnetosphere are organized by
 130 two electric fields: the co-rotation and the dawn-dusk electric fields. The co-rotation
 131 electric field arises from the rotation of Earth's magnetic field. Since particles are
 132 frozen on magnetic field lines and the plasma conductivity is effectively infinite, to a
 133 non-rotating observer, Earth's rotation appears as a radial electric field that drops off
 134 as $\sim L^2$. This electric field makes particles orbit around the Earth due to the $\vec{E} \times \vec{B}$
 135 drift. The other electric field, pointing from dawn to dusk is called the convection
 136 electric field and is due to the Earthward transport of particles from the magnetotail
 137 that appears as an electric field to a stationary observer (with respect to Earth). The
 138 superposition of the co-rotation and convection electric fields results in a potential
 139 field shown in Fig. 1.5. The shaded area in Fig. 1.5 shows the orbits on which low
 140 energy electrons are trapped, and outside are the untrapped particles. The dynamic
 141 topology of the shaded region in Fig. 1.5 is controlled by only the convection electric
 142 field which is dependent on the solar wind speed and the IMF. The lowest energy
 143 particles, that are most effected by these electric fields, make up the plasmasphere.

144 Plasmasphere The plasmasphere is a dense ($n_e \sim 10^3/\text{cm}^3$), cool plasma
 145 ($\sim \text{eV}$) that extends to $L \sim 4$ (extent is highly dependent on the solar wind and
 146 magnetospheric conditions) and is sourced from the ionosphere. The two main
 147 mechanisms that source the cold plasma from the ionosphere are ultraviolet ionization
 148 by sunlight and particle precipitation. The ultraviolet ionization by sunlight is
 149 strongly dependent on the time of day (day vs night), latitude (more ionization near
 150 the equator). The ionization due to particle precipitation, on the other hand, is highly
 151 dependent on magnetospheric conditions, and mostly occurs at high latitudes.

152 The outer boundary of the plasmasphere is the plasmapause which is typically
 153 identified as a steep radial gradient in plasma density from $\sim 10^3/\text{cm}^3$ to $\sim 1/\text{cm}^3$. As

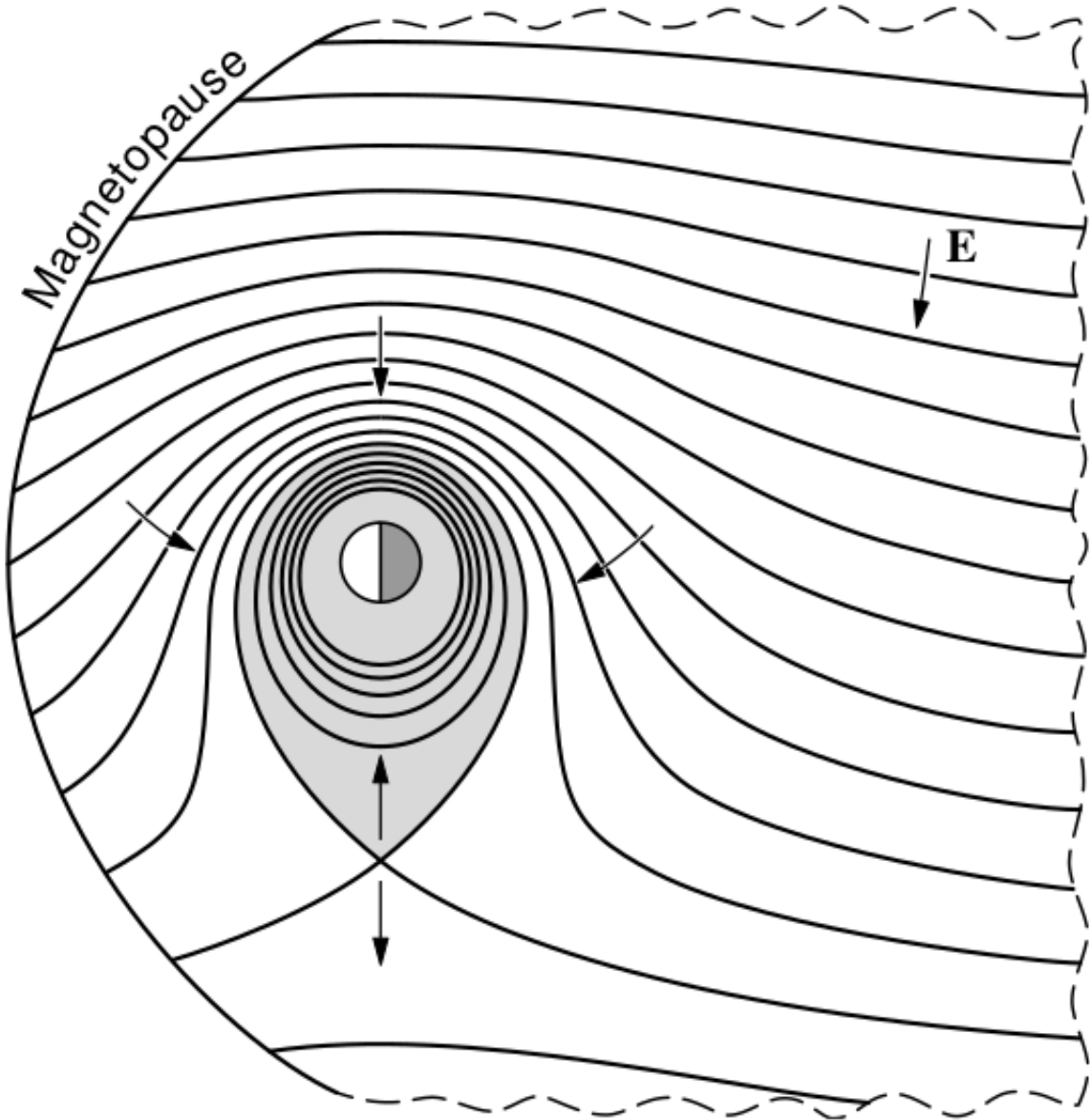


Figure 1.5: Equipotential lines and electric field arrows due to the superposition of the co-rotation and convection electric fields. Electrons in the shaded region execute closed orbits. Outside of the shaded regions the electrons are not trapped and will escape. The region separating the two regimes is called the Alfvén layer. Figure from Baumjohann and Treumann (1997).

₁₅₄ we will see throughout this dissertation, the location of the plasmapause is important
₁₅₅ to model (e.g. O'Brien and Moldwin, 2003) and understand since the plasma density
₁₅₆ strongly controls the efficiency of particle scattering (Horne et al., 2005).

₁₅₇ Ring Current The next higher energy population is the ring current. This
₁₅₈ population consists of protons and electrons between tens and a few hundred keV
₁₅₉ that drift around the Earth. The orbits of higher energy particles are not as effected
₁₆₀ by the convection and co-rotation electric field, rather they drift around the Earth
₁₆₁ due to gradient and curvature drifts. Since the direction of the drift is dependent on
₁₆₂ charge, protons drift west around the Earth and electrons drift East. This has the
₁₆₃ effect of creating a current around the Earth.

₁₆₄ The ring current generates a magnetic field which decreases the magnetic field
₁₆₅ strength on Earth's surface and increases it outside of the ring current. The decrease
₁₆₆ of Earth's magnetic field strength is readily observed by a system of ground-based
₁₆₇ magnetometers and is merged into a Disturbance Storm Time (DST) index. An
₁₆₈ example of a DST index time series from a coronal mass ejection (CME) driven 2015
₁₆₉ St. Patrick's Day storm is shown in Fig. 1.6. The ring current is sometimes first
₁₇₀ depleted and DST increases slightly (initial phase or sudden storm commencement).
₁₇₁ Then the ring current is rapidly built up during which DST rapidly decreases (main
₁₇₂ phase). Lastly the ring current gradually decays toward its equilibrium state over a
₁₇₃ period of a few days and DST increases towards 0 (recovery phase). The DST index
₁₇₄ along with other indicies are readily used by the space physics community to quantify
₁₇₅ the global state of the magnetosphere.

₁₇₆ Radiation Belts The highest energy particle populations are in the Van Allen
₁₇₇ radiation belts. These belts were discovered by Van Allen (1959) and Vernov and
₁₇₈ Chudakov (1960) during the Cold War and are a pair of toroidally shaped populations

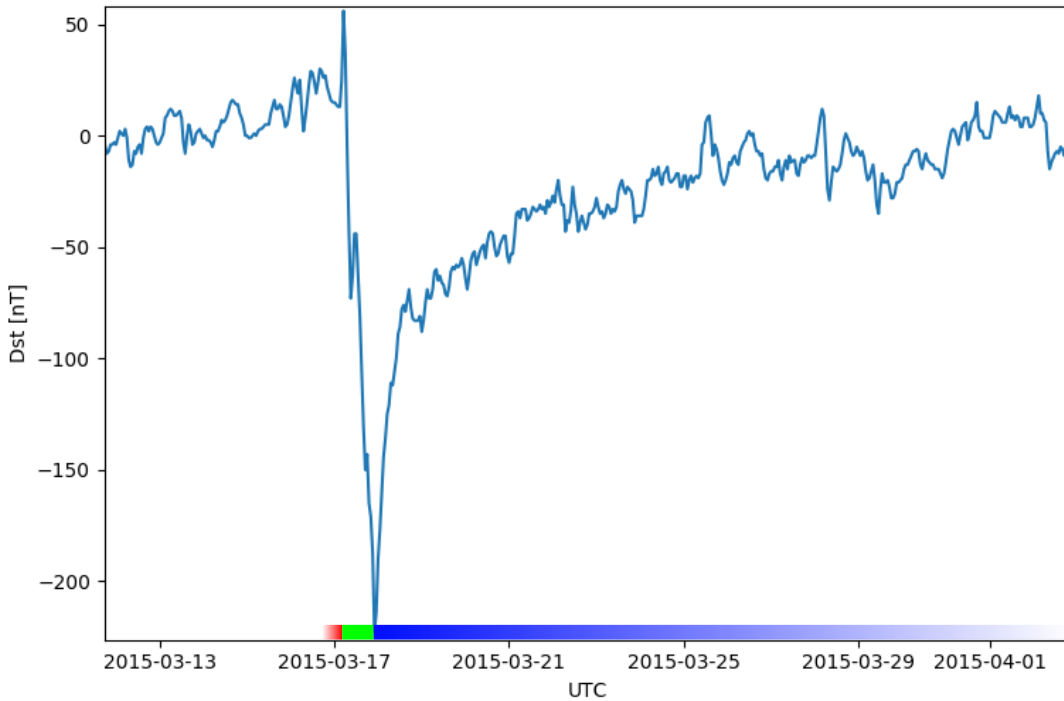


Figure 1.6: The DST index during the St. Patrick's Day 2015 storm. This storm was caused by a coronal mass ejection on March 15th, 2015. The storm phases are: initial phase, main phase, and recovery phase. The initial phase occurred when the Dst peaked at +50 nT on March 17th during which the ring current was eroded by the coronal mass ejection during the interval shown by the red bar. Then the rapid decrease to ≈ -200 nT was during the main phase where many injections from the magnetotail pumped up the ring current which reduced Earth's magnetic field strength at the ground and is shown with the green bar. Lastly, the recovery phase lasted from March 18th to approximately March 29th during which the ring current particles were lost and the ring current returned to its equilibrium state. The recovery phase is shown with the blue bar.

The Earth's Electron Radiation Belts

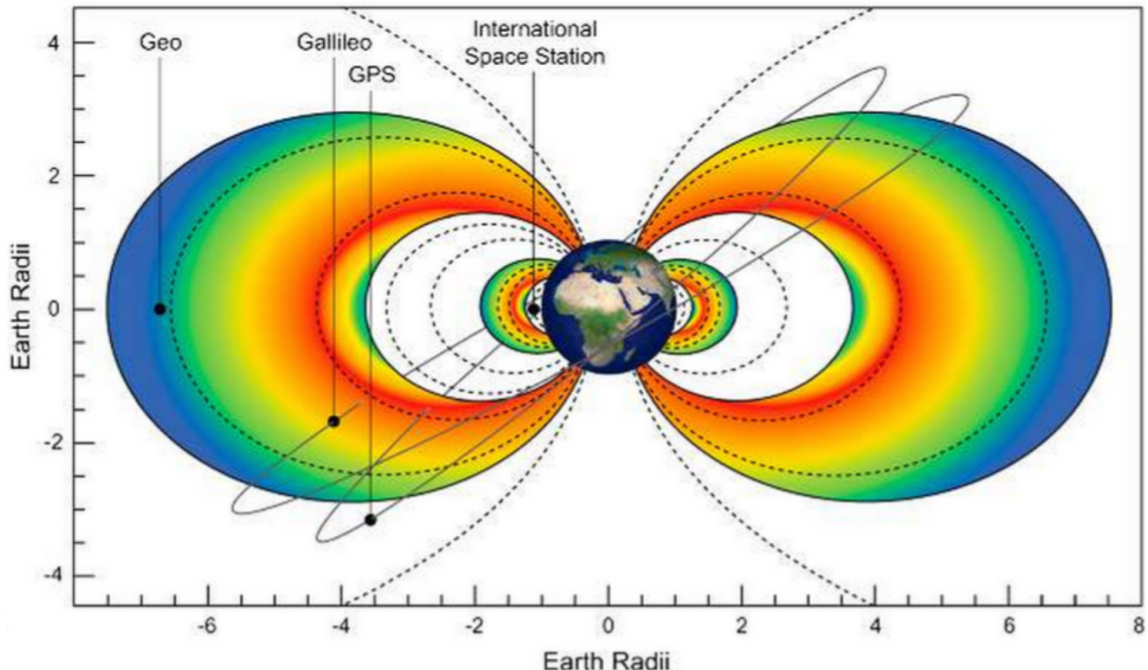


Figure 1.7: The two radiation belts with the locations of various satellites and orbits. Figure from (Horne et al., 2013).

¹⁷⁹ of trapped electrons and protons usually within to $L < 8$ and are shown in Fig. 1.7.
¹⁸⁰ Their quiescent toroidal shape is similar to the shape of the plasmasphere and ring
¹⁸¹ current and is a result of Earth's dipole magnetic field and the conservation of the
¹⁸² three adiabatic invariants discussed in section 1.

¹⁸³ The inner radiation belt is extremely stable on time periods of years, extends
¹⁸⁴ to $L \approx 2$, and mainly consists of protons with energies between MeV and GeV and
¹⁸⁵ electrons with energies up to ≈ 1 MeV (Claudepierre et al., 2019). The source of
¹⁸⁶ inner radiation belt protons is believed to be due to cosmic-ray albedo neutron decay
¹⁸⁷ (e.g. Li et al., 2017) and inward radial diffusion for electrons (e.g. O'Brien et al.,
¹⁸⁸ 2016). The gap between the inner and outer radiation belt is called the slot, which is
¹⁸⁹ believed to be due to hiss waves inside the plasmasphere (described below) scattering

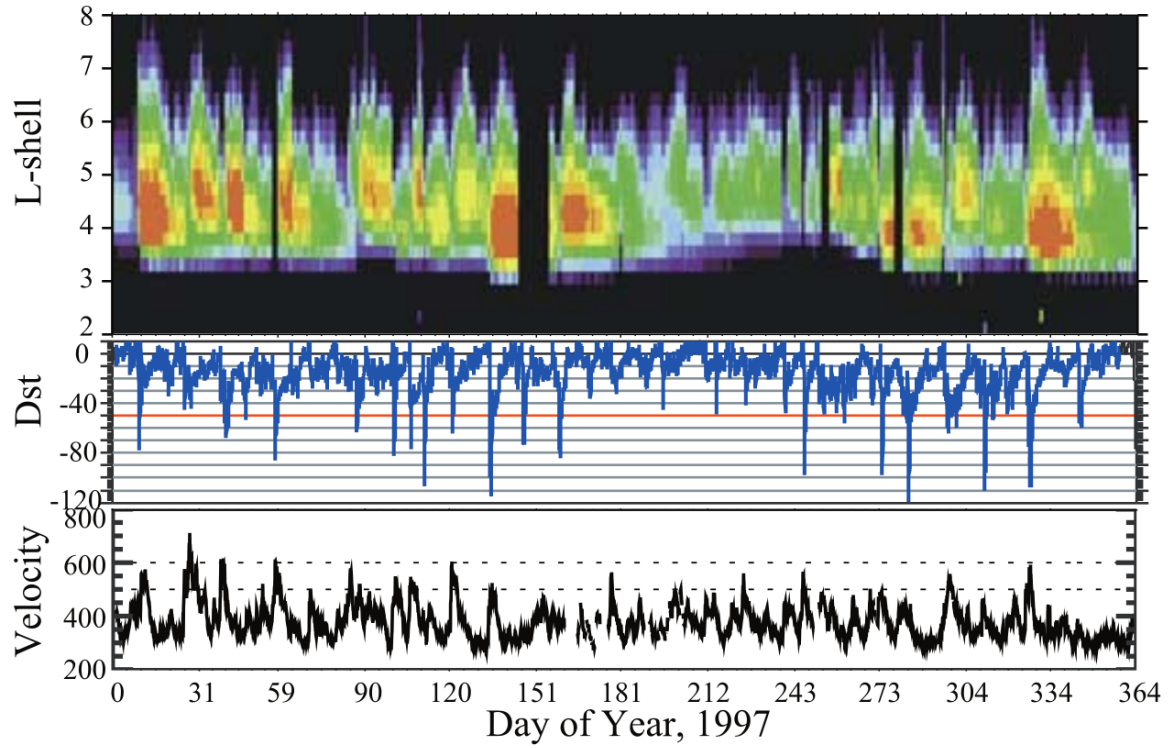


Figure 1.8: The dynamics of the outer radiation belt in 1997 from the POLAR satellite. Top panel shows the 1.2-2.4 MeV electron flux as a function of L and 1997 day of year. The middle panel shows the DST index, and bottom panel shows the solar wind velocity. Figure from (Reeves et al., 2003).

¹⁹⁰ particles into the atmosphere (e.g. Breneman et al., 2015; Lyons and Thorne, 1973).

¹⁹¹ The outer radiation belt, on the other hand is much more dynamic and consists
¹⁹² of mainly electrons of energies up to a few MeV. The outer belt's spatial extent is
¹⁹³ highly variable e.g. see Fig. 1.8, and is typically observed at $4 < L < 8$. Since
¹⁹⁴ the outer radiation belt contains a dynamic population of energetic particles that
¹⁹⁵ pose a threat to human and technological presence in Earth's atmosphere and space,
¹⁹⁶ decades of research has been undertaken to understand and predict the outer radiation
¹⁹⁷ belt particles, waves, and wave-particle interactions. The dynamics of the outer
¹⁹⁸ radiation belt can be understood by considering various competing acceleration and
¹⁹⁹ loss mechanisms which will be described in the following sections.

²⁰⁰

Radiation Belt Particle Sources and Sinks

²⁰¹ Adiabatic Heating

²⁰² One of the particle heating and transport mechanisms arises from the Earthward
²⁰³ convection of particles. The conservation of J_1 implies that the initial and final v_\perp
²⁰⁴ depends on the change in the magnetic field amplitude

$$\frac{v_{\perp i}^2}{B_i} = \frac{v_{\perp f}^2}{B_f}. \quad (1.12)$$

²⁰⁵ As a particle convets Earthward, $B_f > B_i$ thus v_\perp must increase. The dipole
²⁰⁶ magnetic field amplitude can be written as

$$B(L, \theta) = \frac{31.2 \mu\text{T}}{L^3} \sqrt{1 + 3 \cos^2 \theta} \quad (1.13)$$

²⁰⁷ which implies that

$$\frac{v_{\perp f}^2}{v_{\perp i}^2} = \left(\frac{L_i}{L_f}\right)^3. \quad (1.14)$$

²⁰⁸ .

²⁰⁹ In addition, as the particle convects Earthward the distance between the
²¹⁰ particle's mirror points decrease. If J_2 is conserved, the shrinking bounce path implies
²¹¹ that $v_{||}$ must increase by

$$\frac{v_{|| f}^2}{v_{|| i}^2} = \left(\frac{L_i}{L_f}\right)^k \quad (1.15)$$

²¹² where k ranges from 2 for equatorial pitch angles, $\alpha_{eq} = 0^\circ$, to 2.5 for $\alpha_{eq} = 90^\circ$
²¹³ (Baumjohann and Treumann, 1997). Since the rate of adiabatic heating is greater in
²¹⁴ the perpendicular direction than heating in the parallel direction, an initially isotropic
²¹⁵ particle distribution will become anisotropic during its convection. These isotropic
²¹⁶ particles can then become unstable to wave growth and generate waves in order to
²¹⁷ reach equilibrium.

²¹⁸ Wave Resonance Heating

²¹⁹ Another mechanism that heats particles is due to particles resonating with
²²⁰ plasma waves. A few of the electromagnetic wave modes responsible for particle
²²¹ acceleration (and deceleration) relevant to radiation belt dynamics are hiss, whistler
²²² mode chorus (chorus), and electromagnetic ion cyclotron (EMIC) waves. These waves
²²³ are created by the loss cone instability that driven by an anisotropy of electrons
²²⁴ for chorus waves, and protons for EMIC waves. The level of anisotropy can be
²²⁵ quantified by the ratio of the perpendicular to parallel particle temperatures ($T_{\perp}/T_{||}$).
²²⁶ A particle distribution is unstable when $T_{\perp}/T_{||} > 1$ which facilitates wave growth.

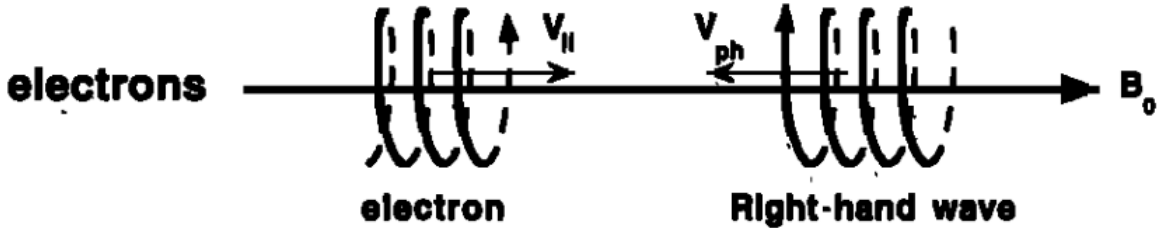


Figure 1.9: The trajectories of an electron and a right-hand circularly polarized wave during a cyclotron resonance. The electron's v_{\parallel} and the wave's k_{\parallel} are in opposite directions such that the wave's frequency is Doppler shifted to an integer multiple of the electron cyclotron frequency. Figure from (Tsurutani and Lakhina, 1997).

227 Since electrons gyrate in a right-handed sense, the chorus waves also tend to be right
 228 hand circularly polarized (Tsurutani and Lakhina, 1997). The same argument applies
 229 to protons and left hand circularly polarized EMIC waves as well.

230 These circularly polarized waves can resonate with electrons and/or protons
 231 when their combined motion results in a static \vec{E} . One example of a resonance
 232 between a right hand circularly polarized wave and an electron is shown in Fig. 1.21
 233 and is termed the cyclotron resonance. An electron's v_{\parallel} and the wave's parallel wave
 234 vector, k_{\parallel} are in opposite directions such that the wave frequency ω is Doppler shifted
 235 to an integer multiple of the Ω_e at which point the electron feels a static electric
 236 field and is accelerated or decelerated. This acceleration happens when a resonance
 237 condition is satisfied between a wave and a particle for which we will now derive an
 238 illustrative toy model.

239 Assume a uniform magnetic field $\vec{B} = B_0 \hat{z}$ with a parallel propagating ($k = k \hat{z}$),
 240 right-hand circularly polarized wave. The wave's electric field as a function of position
 241 and time can be written as

$$\vec{E} = E_0 (\cos(\omega t - kz) \hat{x} + \sin(\omega t - kz) \hat{y}) \quad (1.16)$$

which is more clearly expressed by taking the dot product to find \vec{E} in the $\hat{\theta}$ direction

$$E_\theta = \vec{E} \times \hat{\theta} = E_0 \cos(\omega t - kz + \theta). \quad (1.17)$$

²⁴² Now assume that the electron is traveling in the $-\hat{z}$ direction with a velocity $\vec{v} = -v_0 \hat{z}$
²⁴³ so its time dependent position along \hat{z} is

$$z(t) = -v_0 t \quad (1.18)$$

²⁴⁴ and gyrophase is

$$\theta(t) = -\Omega t + \theta(0) \quad (1.19)$$

²⁴⁵ where the first negative sign comes from the electron's negative charge. Now we put
²⁴⁶ this all together and express the electric field and the force that the electron will
²⁴⁷ experience

$$m \frac{dv_\theta}{dt} = qE_\theta = qE_0 \sin((\omega + kv_0 - \Omega)t + \theta(0)). \quad (1.20)$$

²⁴⁸ This is a relatively complex expression, but when the time dependent component,

$$\omega + kv_0 - \Omega = 0, \quad (1.21)$$

²⁴⁹ the electron will be in a static electric field which will accelerate or decelerate the
²⁵⁰ electron depending on θ_0 , the phase between the wave and the electron. **Show Bortnik
²⁵¹ 2008 plot?** The expression in Eq. 1.21 is commonly referred to as the resonance

252 condition and is more generally written as

$$\omega - k_{||}v_{||} = \frac{n\Omega_e}{\gamma} \quad (1.22)$$

253 where n is the resonance order, and γ is the relativistic correction (e.g. Millan and
254 Thorne, 2007). In the case of the cyclotron resonance, $\omega \approx \Omega_e$ thus J_1 is violated.
255 Since J_1 is violated, J_2 and J_3 are also violated since the conditions required to
256 violate J_2 and J_3 are less stringent than J_1 . It is important to remember that along
257 the particle's orbit it will encounter and experience the effects of many waves along
258 its orbit. The typical MLT extent of a handful of waves that are capable of resonating
259 with radiation belt electrons are shown in Fig. 1.10.

260 Particle Losses

261 Now that we have seen two general mechanisms with which particles are
262 accelerated and transported in the magnetosphere, we will now consider a few
263 specific mechanisms with which particles are lost to the atmosphere or the solar
264 wind. One particle loss mechanism into the solar wind is magnetopause shadowing
265 (e.g. Ukhorskiy et al., 2006). Particles are sometimes lost when the ring current is
266 strengthened and Earth's magnetic field strength is increased outside of the ring
267 current (and reduced on Earth's surface). If the time scale of the ring current
268 strengthening is slower than a particle drift, J_3 is conserved. Then in order to
269 conserve J_3 while the magnetic field strength is increased, the particle's drift shell
270 must move outward to conserve the magnetic flux contained by the drift shell. Then
271 if the particle's drift shell expands to the point that it crosses the magnetopause, the
272 particle will be lost to the solar wind.

273 **Move to acceleration?** Another particle loss and acceleration mechanism is driven
274 by ultra low frequency (ULF) waves and is called radial diffusion. Radial diffusion is

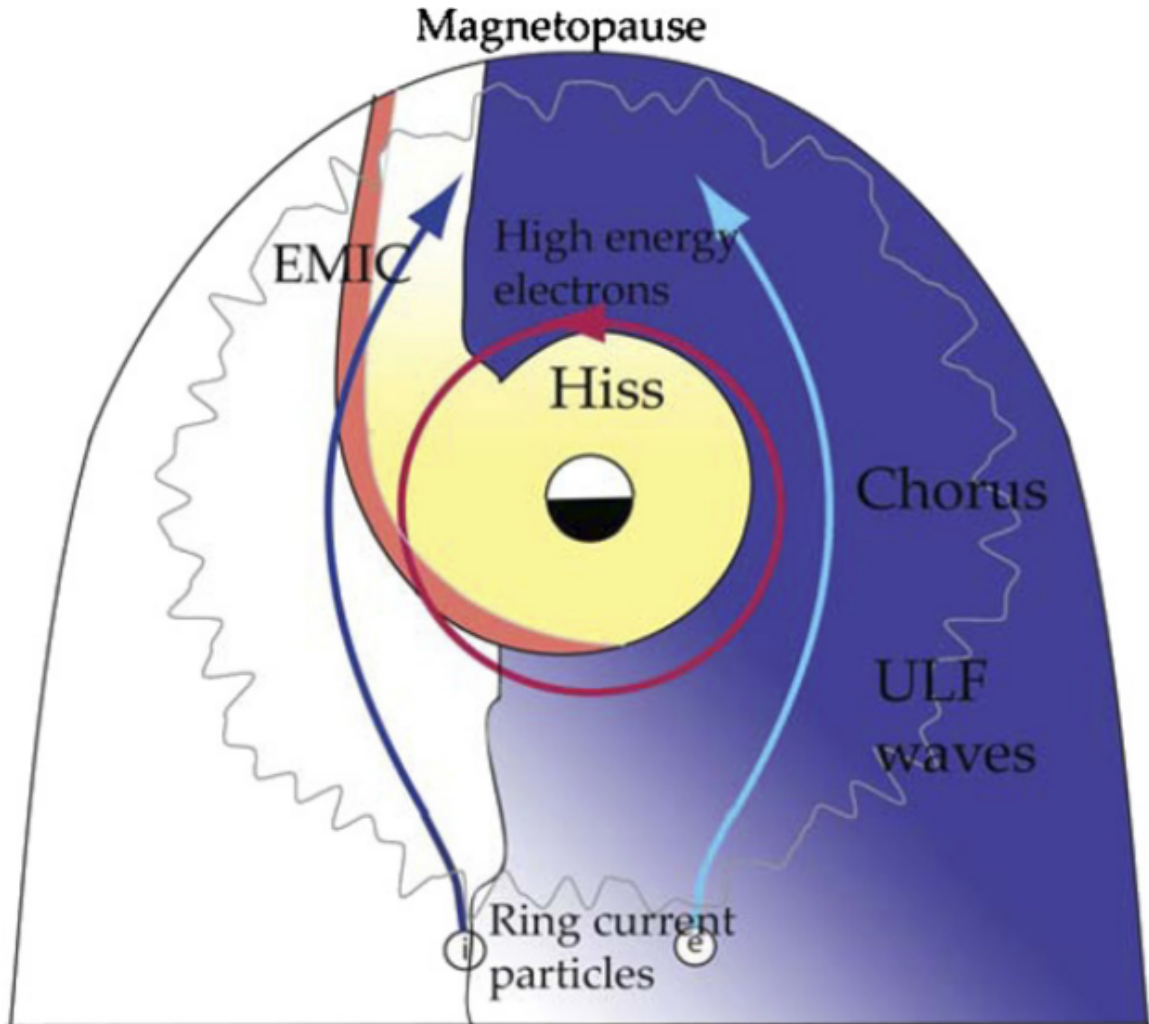


Figure 1.10: Various wave modes in the magnetosphere. Ultra low frequency waves occur through the magnetosphere. Chorus waves are typically observed in the 0-12 midnight-dawn region. EMIC waves are typically observed in the dusk MLT sector. Hiss waves are observed inside the plasmasphere. Figure from Millan and Thorne (2007).

275 the transport of particles from high to low phase space density, f . If the transport is
 276 radially inward, particles will appear to be accelerated. On the other hand, radially
 277 outward radial diffusion can transport particles through the magnetopause where
 278 they will be lost to the solar wind. Reeves et al. (2013) investigated the driver of
 279 particle acceleration during the October 2012 storm and observationally found that
 280 inward radial diffusion was not dominant, rather local acceleration via wave-resonance
 281 heating (i.e. particle diffusion in pitch angle and energy which will be described below)
 282 appeared to be the dominant acceleration mechanism.

283 The loss mechanism central to this dissertation is pitch angle and energy
 284 scattering of electrons by waves. Some of the waves that scatter electrons in energy
 285 and pitch angle in the inner magnetosphere are: plasmaspheric hiss (e.g. Breneman
 286 et al., 2015; O'Brien et al., 2014), EMIC waves (e.g. Capannolo et al., 2019; Hendry
 287 et al., 2017), and chorus waves (e.g. Breneman et al., 2017; Kasahara et al., 2018;
 288 Ozaki et al., 2019). These wave-particle interactions occur when the resonance
 289 condition in Eq. 1.22 is satisfied at which point the particle's energy and α is modified
 290 by the wave. More details regarding the theory of pitch angle and energy diffusion is
 291 given in Chapter X. If the wave changes α towards 0 such that $\alpha < \alpha_{LC}$, the particle's
 292 mirror point lowers to less than 100 km altitude where the particle can be lost due
 293 collisions with air. One manifestation of pitch angle scattering of particles into the
 294 loss cone are microbursts: a sub-second durtation impulse of electrons.

295

Microbursts

296 Microbursts were first identified in high altitude balloon observations of bremsstrahlung
 297 X-rays emitted by microburst electrons impacting the atmosphere by Anderson and
 298 Milton (1964). Since then, other balloons have observed microburst X-ray signatures
 299 in the upper atmosphere (e.g. Anderson et al., 2017; Barcus et al., 1966; Parks, 1967;

300 Trefall et al., 1966; Woodger et al., 2015; ?). In addition to their X-ray signature,
 301 microbursts electrons have been directly observed in LEO with spacecraft including
 302 the Solar Anomalous and Magnetospheric Particle Explorer (SAMPEX), Focused
 303 Investigation of Relativistic Electron Bursts: Intensity, Range, and Dynamics II
 304 (FIREBIRD-II), Science Technologies Satellite (STSAT-I) (e.g. Blake et al., 1996;
 305 Blum et al., 2015; Breneman et al., 2017; Crew et al., 2016; Lee et al., 2012, 2005;
 306 Lorentzen et al., 2001a,b; Nakamura et al., 1995, 2000; O'Brien et al., 2004, 2003).
 307 An example microburst time series is shown in Fig. 1.11 and was observed by
 308 Montana State University's (MSU) FIREBIRD-II CubeSats. The prominent features
 309 of microbursts in Fig. 1.11 are their ≈ 1 second duration, half order of magnitude
 310 increase in count rate above the falling background, and their approximately 200-800
 311 keV energy extent.

312 Microbursts are observed on magnetic field footprints that are connected to the
 313 outer radiation belt (approximately $4 < L < 8$), and are predominately observed in
 314 the 0-12 MLT sector with an elevated occurrence frequency during magnetospherically
 315 disturbed times as shown in Fig. 1.12. Microbursts have been previously observed
 316 over a wide energy range from a few tens of keV (Datta et al., 1997; Parks, 1967) to
 317 greater than 1 MeV (e.g. Blake et al., 1996; Greeley et al., 2019). The microburst
 318 electron flux (J) falls off in energy, and the microburst energy spectra is typically
 319 well fit to a decaying exponential

$$J(E) = J_0 e^{-E/E_0} \quad (1.23)$$

320 where J_0 is the flux at 0 keV (unphysical free parameter) and E_0 quantifies the
 321 efficiency of the scattering mechanism in energy (.e.g Datta et al., 1997; Lee et al.,
 322 2005; Parks, 1967). A small E_0 suggests that mostly low energy particles are scattered

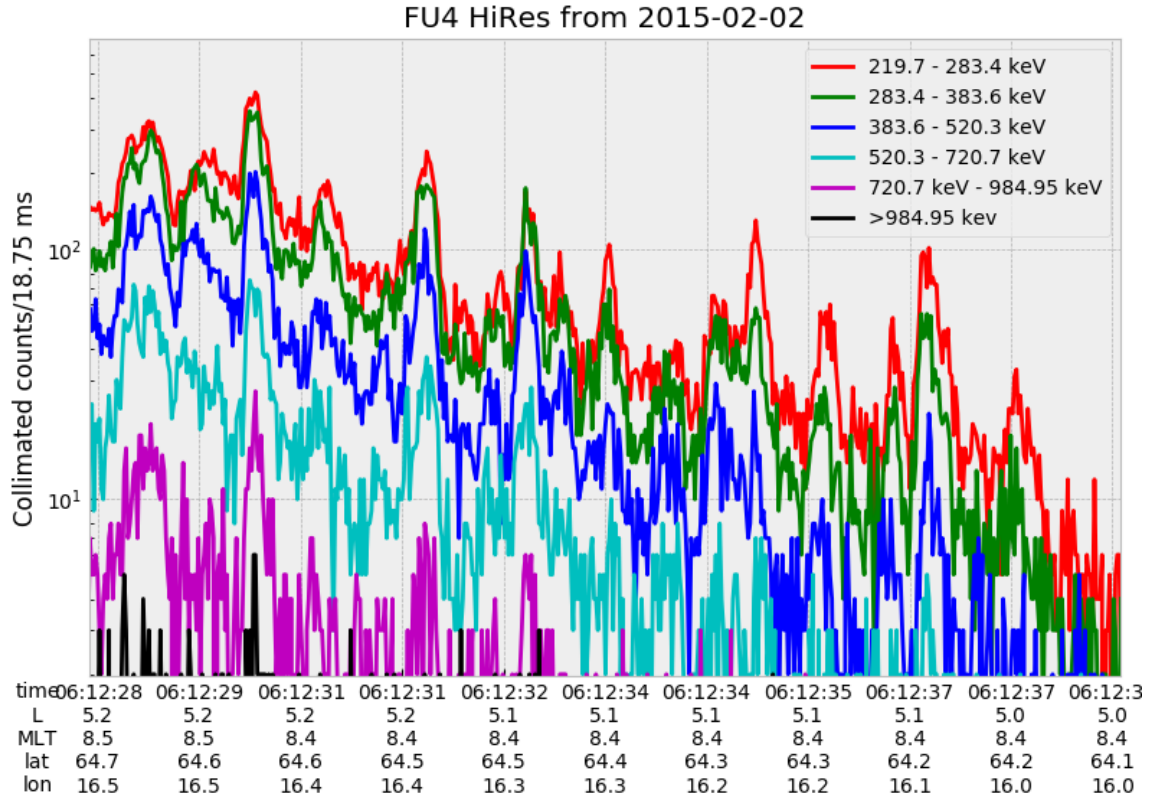


Figure 1.11: An example train of microbursts observed by FIREBIRD-II unit 4 on February 2nd, 2015. The colored curves show the differential energy channel count rates in six channels from ≈ 200 keV to greater than 1 MeV. The x-axis labels show auxiliary information such as time of observation and the spacecraft position in L, MLT, latitude and longitude coordinates.

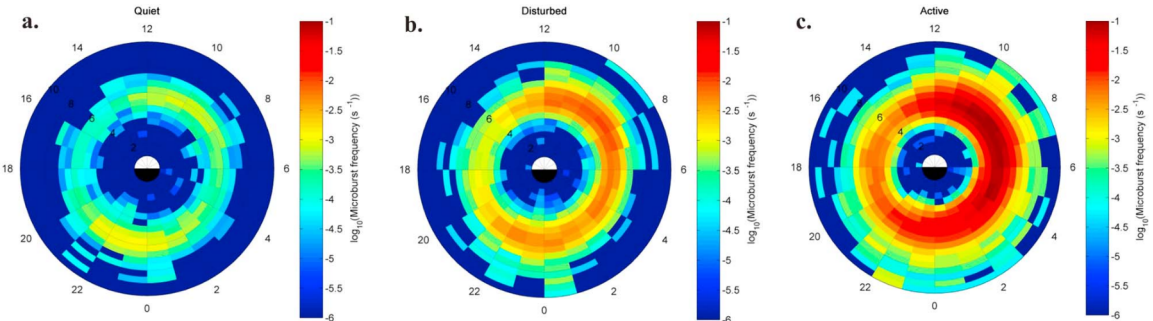


Figure 1.12: Relativistic ($> 1\text{MeV}$) distribution of microburst occurrence rates as a function of L and MLT. The three panels show the microburst occurrence rate dependence on geomagnetic activity, parameterized by the auroral electrojet (AE) index for (a) $\text{AE} < 100 \text{nT}$, (b) $100 < \text{AE} < 300 \text{nT}$ and (c) $\text{AE} > 300 \text{nT}$. Figure from Douma et al. (2017).

and a high E_0 suggests that the scattering mechanism scatters low and high energy electrons. Reality is a bit more messy and a high E_0 may be a signature of a scattering mechanism preferential to high energy electrons, but is hidden by the convolution of the source particles available to be scattered (typically with a falling energy spectrum) and the energy-dependent scattering efficiency.

The short duration of microbursts observed by a single LEO satellite has an ambiguity when interpreting what is exactly a microburst. The two possible realities are: a microburst is very small and spatially stationary so that the LEO spacecraft passes through it in less than a second. Alternatively, microbursts are spatially large with a short duration such that the microburst passes by the spacecraft in a fraction of a second. There are a few ways to distinguish between the two possible realities, and each one has a unique set of advantages.

A high altitude balloon provides essentially a stationary view of the precipitating particles under the radiation belt footprints so a short-lived, temporal microburst can be unambiguously identified. Spatial structures on the other hand are difficult to identify because a balloon is essentially still on drift timescales thus a variation in

339 the X-rays can be due to the spatial structure or an increase of precipitating particles
 340 over the whole area. Furthermore, if the stationary structure is drifting its particles
 341 are not precipitating into the atmosphere so there is no X-ray signature.

342 Another solution is multi-spacecraft missions that can determine if a microburst
 343 is spatial or temporal. As will be shown in this dissertation, if a microburst is
 344 observed simultaneously by two spacecraft then it is temporally transient and has
 345 a size greater than the spacecraft separation. On the other hand, if two spacecraft
 346 observe a microburst-like feature in the same location and at different times, then it is
 347 spatial may be a curtain (Blake and O'Brien, 2016). Both observational methods have
 348 a unique set of strengths, and this dissertation takes the multi-spacecraft approach
 349 to identify and study microbursts.

350

Scope of Reserach

351 This dissertation furthers our understanding of the microburst scattering
 352 mechanism by observing the scattering directly, and measuring the microburst sizes
 353 and comparing them to the size of waves near the magnetic equator where those
 354 electrons could have been scattered. Chapter **X** describes a microburst scattering
 355 event observed by NASA's Van Allen Probes which was studied in the theoretic
 356 framework of pitch angle and energy diffusion. The following two chapters will then
 357 study the size of microbursts. Chapter **Y** describes a bouncing packet microburst
 358 observation made by MSU's FIREBIRD-II mission where the microburst's lower
 359 bound longitudinal and latitudinal sizes were estimated. Then Chapter **Z** expands
 360 the case study from Ch. **Y** to a statistical study of microburst sizes using The
 361 Aerospace Corporation's AeroCube-6 (AC6) CubeSats. In this study, a Monte Carlo
 362 and analytic microburst size models were developed to account for the compounding
 363 effects of random microburst sizes and locations. Lastly, Ch. **A** will summarize the

³⁶⁴ dissertation work and make concluding remarks regarding outstanding questions in
³⁶⁵ microburst physics.

- 367 Anderson, B., Shekhar, S., Millan, R., Crew, A., Spence, H., Klumpar, D., Blake, J.,
 368 O'Brien, T., and Turner, D. (2017). Spatial scale and duration of one microburst
 369 region on 13 August 2015. *Journal of Geophysical Research: Space Physics*.
- 370 Anderson, K. A. and Milton, D. W. (1964). Balloon observations of X rays in the
 371 auroral zone: 3. High time resolution studies. *Journal of Geophysical Research*,
 372 69(21):4457–4479.
- 373 Barcus, J., Brown, R., and Rosenberg, T. (1966). Spatial and temporal character of
 374 fast variations in auroral-zone x rays. *Journal of Geophysical Research*, 71(1):125–
 375 141.
- 376 Baumjohann, W. and Treumann, R. A. (1997). *Basic space plasma physics*. World
 377 Scientific.
- 378 Blake, J.,Looper, M., Baker, D., Nakamura, R., Klecker, B., and Hovestadt, D.
 379 (1996). New high temporal and spatial resolution measurements by sampex of the
 380 precipitation of relativistic electrons. *Advances in Space Research*, 18(8):171 – 186.
- 381 Blake, J. B. and O'Brien, T. P. (2016). Observations of small-scale latitudinal
 382 structure in energetic electron precipitation. *Journal of Geophysical Research: Space
 383 Physics*, 121(4):3031–3035. 2015JA021815.
- 384 Blum, L., Li, X., and Denton, M. (2015). Rapid MeV electron precipitation as
 385 observed by SAMPEX/HILT during high-speed stream-driven storms. *Journal of
 386 Geophysical Research: Space Physics*, 120(5):3783–3794. 2014JA020633.
- 387 Breneman, A., Crew, A., Sample, J., Klumpar, D., Johnson, A., Agapitov, O.,
 388 Shumko, M., Turner, D., Santolik, O., Wygant, J., et al. (2017). Observations
 389 directly linking relativistic electron microbursts to whistler mode chorus: Van allen
 390 probes and FIREBIRD II. *Geophysical Research Letters*.
- 391 Breneman, A. W., Halford, A., Millan, R., McCarthy, M., Fennell, J., Sample, J.,
 392 Woodger, L., Hospodarsky, G., Wygant, J. R., Cattell, C. A., et al. (2015). Global-
 393 scale coherence modulation of radiation-belt electron loss from plasmaspheric hiss.
 394 *Nature*, 523(7559):193.
- 395 Capannolo, L., Li, W., Ma, Q., Shen, X.-C., Zhang, X.-J., Redmon, R., Rodriguez,
 396 J., Engebretson, M., Kletzing, C., Kurth, W., et al. (2019). Energetic electron
 397 precipitation: multi-event analysis of its spatial extent during emic wave activity.
 398 *Journal of Geophysical Research: Space Physics*.
- 399 Claudepierre, S., O'Brien, T., Looper, M., Blake, J., Fennell, J., Roeder, J.,
 400 Clemmons, J., Mazur, J., Turner, D., Reeves, G., et al. (2019). A revised look

- 401 at relativistic electrons in the earth's inner radiation zone and slot region. *Journal
402 of Geophysical Research: Space Physics*, 124(2):934–951.
- 403 Crew, A. B., Spence, H. E., Blake, J. B., Klumpar, D. M., Larsen, B. A., O'Brien,
404 T. P., Driscoll, S., Handley, M., Legere, J., Longworth, S., Mashburn, K.,
405 Mosleh, E., Ryhajlo, N., Smith, S., Springer, L., and Widholm, M. (2016). First
406 multipoint in situ observations of electron microbursts: Initial results from the
407 NSF FIREBIRD II mission. *Journal of Geophysical Research: Space Physics*,
408 121(6):5272–5283. 2016JA022485.
- 409 Datta, S., Skoug, R., McCarthy, M., and Parks, G. (1997). Modeling of microburst
410 electron precipitation using pitch angle diffusion theory. *Journal of Geophysical
411 Research: Space Physics*, 102(A8):17325–17333.
- 412 Douma, E., Rodger, C. J., Blum, L. W., and Clilverd, M. A. (2017). Occurrence
413 characteristics of relativistic electron microbursts from SAMPEX observations.
414 *Journal of Geophysical Research: Space Physics*, 122(8):8096–8107. 2017JA024067.
- 415 Eastwood, J., Hietala, H., Toth, G., Phan, T., and Fujimoto, M. (2015). What
416 controls the structure and dynamics of earths magnetosphere? *Space Science
417 Reviews*, 188(1-4):251–286.
- 418 Greeley, A., Kanekal, S., Baker, D., Klecker, B., and Schiller, Q. (2019). Quantifying
419 the contribution of microbursts to global electron loss in the radiation belts. *Journal
420 of Geophysical Research: Space Physics*.
- 421 Hendry, A. T., Rodger, C. J., and Clilverd, M. A. (2017). Evidence of sub-mev
422 emic-driven electron precipitation. *Geophysical Research Letters*, 44(3):1210–1218.
- 423 Horne, R., Glauert, S., Meredith, N., Boscher, D., Maget, V., Heynderickx, D., and
424 Pitchford, D. (2013). Space weather impacts on satellites and forecasting the earth's
425 electron radiation belts with spacecast. *Space Weather*, 11(4):169–186.
- 426 Horne, R. B., Thorne, R. M., Shprits, Y. Y., Meredith, N. P., Glauert, S. A., Smith,
427 A. J., Kanekal, S. G., Baker, D. N., Engebretson, M. J., Posch, J. L., et al.
428 (2005). Wave acceleration of electrons in the van allen radiation belts. *Nature*,
429 437(7056):227.
- 430 Kasahara, S., Miyoshi, Y., Yokota, S., Mitani, T., Kasahara, Y., Matsuda, S.,
431 Kumamoto, A., Matsuoka, A., Kazama, Y., Frey, H., et al. (2018). Pulsating
432 aurora from electron scattering by chorus waves. *Nature*, 554(7692):337.
- 433 Lee, J. J., Parks, G. K., Lee, E., Tsurutani, B. T., Hwang, J., Cho, K. S., Kim, K.-H.,
434 Park, Y. D., Min, K. W., and McCarthy, M. P. (2012). Anisotropic pitch angle
435 distribution of 100 keV microburst electrons in the loss cone: measurements from
436 STSAT-1. *Annales Geophysicae*, 30(11):1567–1573.

- 437 Lee, J.-J., Parks, G. K., Min, K. W., Kim, H. J., Park, J., Hwang, J., McCarthy,
 438 M. P., Lee, E., Ryu, K. S., Lim, J. T., Sim, E. S., Lee, H. W., Kang, K. I., and
 439 Park, H. Y. (2005). Energy spectra of 170–360 keV electron microbursts measured
 440 by the korean STSAT-1. *Geophysical Research Letters*, 32(13). L13106.
- 441 Li, X., Selesnick, R., Schiller, Q., Zhang, K., Zhao, H., Baker, D. N., and Temerin,
 442 M. A. (2017). Measurement of electrons from albedo neutron decay and neutron
 443 density in near-earth space. *Nature*, 552(7685):382.
- 444 Lorentzen, K. R., Blake, J. B., Inan, U. S., and Bortnik, J. (2001a). Observations
 445 of relativistic electron microbursts in association with VLF chorus. *Journal of
 446 Geophysical Research: Space Physics*, 106(A4):6017–6027.
- 447 Lorentzen, K. R.,Looper, M. D., and Blake, J. B. (2001b). Relativistic electron
 448 microbursts during the GEM storms. *Geophysical Research Letters*, 28(13):2573–
 449 2576.
- 450 Lyons, L. R. and Thorne, R. M. (1973). Equilibrium structure of radiation belt
 451 electrons. *Journal of Geophysical Research*, 78(13):2142–2149.
- 452 Millan, R. and Thorne, R. (2007). Review of radiation belt relativistic electron losses.
 453 *Journal of Atmospheric and Solar-Terrestrial Physics*, 69(3):362 – 377.
- 454 Nakamura, R., Baker, D. N., Blake, J. B., Kanekal, S., Klecker, B., and Hovestadt,
 455 D. (1995). Relativistic electron precipitation enhancements near the outer edge of
 456 the radiation belt. *Geophysical Research Letters*, 22(9):1129–1132.
- 457 Nakamura, R., Isowa, M., Kamide, Y., Baker, D., Blake, J., and Looper, M. (2000).
 458 Observations of relativistic electron microbursts in association with VLF chorus.
 459 *J. Geophys. Res*, 105:15875–15885.
- 460 O'Brien, T., Claudepierre, S., Blake, J., Fennell, J. F., Clemons, J., Roeder, J.,
 461 Spence, H. E., Reeves, G., and Baker, D. (2014). An empirically observed pitch-
 462 angle diffusion eigenmode in the earth's electron belt near $l^* = 5.0$. *Geophysical
 463 Research Letters*, 41(2):251–258.
- 464 O'Brien, T., Claudepierre, S., Guild, T., Fennell, J., Turner, D., Blake, J., Clemons,
 465 J., and Roeder, J. (2016). Inner zone and slot electron radial diffusion revisited.
 466 *Geophysical Research Letters*, 43(14):7301–7310.
- 467 O'Brien, T. and Moldwin, M. (2003). Empirical plasmapause models from magnetic
 468 indices. *Geophysical Research Letters*, 30(4).
- 469 O'Brien, T. P., Looper, M. D., and Blake, J. B. (2004). Quantification of relativistic
 470 electron microburst losses during the GEM storms. *Geophysical Research Letters*,
 471 31(4). L04802.

- 472 O'Brien, T. P., Lorentzen, K. R., Mann, I. R., Meredith, N. P., Blake, J. B., Fennell,
 473 J. F., Looper, M. D., Milling, D. K., and Anderson, R. R. (2003). Energization of
 474 relativistic electrons in the presence of ULF power and MeV microbursts: Evidence
 475 for dual ULF and VLF acceleration. *Journal of Geophysical Research: Space
 476 Physics*, 108(A8).
- 477 Ozaki, M., Miyoshi, Y., Shiokawa, K., Hosokawa, K., Oyama, S.-i., Kataoka, R.,
 478 Ebihara, Y., Ogawa, Y., Kasahara, Y., Yagitani, S., et al. (2019). Visualization of
 479 rapid electron precipitation via chorus element wave-particle interactions. *Nature
 480 communications*, 10(1):257.
- 481 Parks, G. K. (1967). Spatial characteristics of auroral-zone X-ray microbursts. *Journal
 482 of Geophysical Research*, 72(1):215–226.
- 483 Reeves, G., Spence, H. E., Henderson, M., Morley, S., Friedel, R., Funsten, H., Baker,
 484 D., Kanekal, S., Blake, J., Fennell, J., et al. (2013). Electron acceleration in the
 485 heart of the van allen radiation belts. *Science*, 341(6149):991–994.
- 486 Reeves, G. D., McAdams, K. L., Friedel, R. H. W., and O'Brien, T. P. (2003). Ac-
 487 celeration and loss of relativistic electrons during geomagnetic storms. *Geophysical
 488 Research Letters*, 30(10):n/a–n/a. 1529.
- 489 Schulz, M. and Lanzerotti, L. J. (1974). *Particle Diffusion in the Radiation Belts*.
 490 Springer.
- 491 Trefall, H., Bjordal, J., Ullaland, S., and Stadsnes, J. (1966). On the extension of
 492 auroral-zone x-ray microbursts. *Journal of Atmospheric and Terrestrial Physics*,
 493 28(2):225–233.
- 494 Tsurutani, B. T. and Lakhina, G. S. (1997). Some basic concepts of wave-particle
 495 interactions in collisionless plasmas. *Reviews of Geophysics*, 35(4):491–501.
- 496 Ukhorskiy, A. Y., Anderson, B. J., Brandt, P. C., and Tsyganenko, N. A. (2006).
 497 Storm time evolution of the outer radiation belt: Transport and losses. *Journal of
 498 Geophysical Research: Space Physics*, 111(A11):n/a–n/a. A11S03.
- 499 Van Allen, J. A. (1959). The geomagnetically trapped corpuscular radiation. *Journal
 500 of Geophysical Research*, 64(11):1683–1689.
- 501 Vernov, S. and Chudakov, A. (1960). Investigation of radiation in outer space. In
 502 *International Cosmic Ray Conference*, volume 3, page 19.
- 503 Woodger, L., Halford, A., Millan, R., McCarthy, M., Smith, D., Bowers, G., Sample,
 504 J., Anderson, B., and Liang, X. (2015). A summary of the BARREL campaigns:
 505 Technique for studying electron precipitation. *Journal of Geophysical Research: Space
 506 Physics*, 120(6):4922–4935.